Graphical abstract

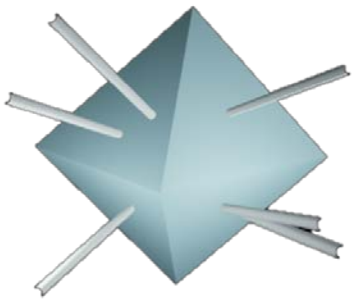

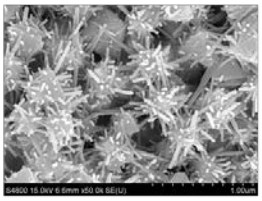

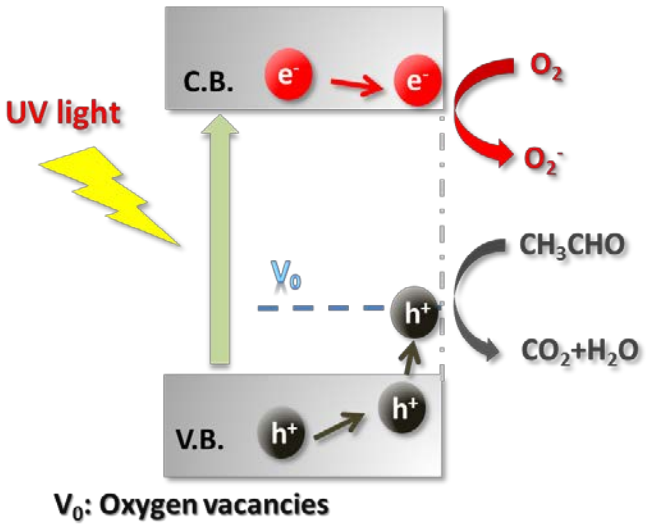

V_0: Oxygen vacancies

Highlights:

1. Yttrium doped hedgehog-like hierarchical structure CeO2 were successfully fabricated for the first time by a facile and template-free approach.

2. Compared with traditional morphology CeO2 nanoparticles, photocatalytic activities of Yttrium doped hedgehog-like hierarchical structure CeO2 were improved obviously.

3. Based on doped and morphology controlled, the oxygen vacancy concentration plays a key impact on the photocatalytic activities of as-fabricated products.

Morphology Control and Photocatalytic Characterization of Yttrium Doped Hedgehog-like CeO_2

Bin Xu [a,b,c], Qitao Zhang [a,b], Saisai Yuan [a,b], Ming Zhang [a,c] *,Teruhisa Ohno[b,d,e,f],*

[a] School of Chemistry and Chemical Engineering, Yangzhou University, Yangzhou 225002, China

[b] Department of Applied Chemistry, Faculty of Engineering, Kyushu Institute of Technology, Kitakyushu 804-8550, Japan

[c] Test Center, Yangzhou University, Yangzhou 225002, China

[d] JST, PRESTO, 4-1-8 Honcho Kawaguchi, Saitama 332-0012, Japan

[e] JST, ACT-C, 4-1-8 Honcho Kawaguchi, Saitama 332-0012, Japan

[f] Research Center for Advanced Eco-fitting Technology, Kyushu Institute of Technology, Tobata, Kitakyushu 804-8550, Japan

*corresponding author. Tel：+81 93 884 3318；Fax: +81 93 884 3318

E-mail address: lxyzhangm@yzu.edu.cn (Ming Zhang)

tohno@che.kyutech.jp (T.Ohno)

Abstract: Yttrium doped hedgehog-like ceria with high concentration of oxygen vacancies were successfully prepared by traditional hydrothermal process. Crystal phase composition, morphology, and size of as-fabricated products were found to be greatly dependent on the mole ratio of origin materials and reaction temperature. The morphology and size of the as-prepared samples was characterized by FE-SEM, HR-TEM and HADDF-STEM. Structure information was obtained by XRD and Raman analysis. Absorption band and band gap energy, which are responsible for the observed photocatalytic behavior, were investigated by UV-vis diffuse reflectance. In addition, the optimum experiment condition for target products was found. The as-prepared doped 3D hierarchical structure samples showed highest photocatalytic activity compared with 1D octahedral and nanorod morphology ceria which evaluated by measuring CO_2 liberation form the photocatalytic decomposition of acetaldehyde.

Keywords: yttrium doped ceria, hierarchical structure, oxygen vacancy, morphology control, photocatalytic activity

1. Introduction

Cerium dioxides, a significant rare-earth oxide, has attracted great attention due to its significant fluorite type structure, remarkable redox properties[1] and prominent oxygen storage and release capacity (OSC) via facile conversion between Ce^{4+} and Ce^{3+} oxidation states[2]. It has been extensively utilized in many practical applications such as polishing materials[3], solar cells[4], ultraviolet blocking materials[5, 6] and photocatalytic materials. Pure CeO_2, an n-type semiconductor, has a similar band gap (3.2eV) with other commonly semiconductor-based photocatalyst such as TiO_2[7] and possesses potential as a suitable photocatalyst. Recently various methods have been widely utilized for the synthesis of CeO_2 with various morphologies such as thermal evaporation[8], coprecipitation[9], and the sol-gel technique[10]. Previously researches have revealed that excellent catalytical performance and easy functionalization of CeO_2 materials have been achieved by controlling their structural properties[11]. For instance, our group have successfully fabricated a sesame ball-like CeO_2: Y3+/P(St-AA) composite microsphere[12].

Compared with conventional nanowires, nanorods and nanocubes as well as nanoparticles with other shapes, newly constructed hierarchical architecture CeO_2 will acquire some special properties that above single morphology CeO_2 does not possess[10, 13, 14]. Although some progress has been made in the fabrication of hierarchical architectures composed of a 1D nanostructure, these methods usually need special templates through a complex experimental course. For example, Sam L. Mitchell et.al had fabricated the coral-like mesostructured CeO_2 using amino acid as template [15]. Zhong et al. reported the preparation of 3D flowerlike ceria at 180 ℃ with TBAB as a surfactant and EG as a solvent[16].

Morphology and size controlled, metal and metal oxide composites and different ionic doping are three most commonly used method which are widely employed in enhancing the photocatalytic properties of the CeO_2-based materials. The most keypoint of these approaches is to changing the oxygen vacancies concentration of products. That's because oxygen vacancies can act as electron or hole capture centers and can trap the photogenerated electrons or holes which excited by ultraviolet or visible light. Further oxygen vacancies can effectively restrain the recombination of electron-hole pairs resulting in improving the photocatalytic activities[17]. More than two or all of above methods applied in the preparation 3D hierarchical structure of CeO_2 with high concentration of oxygen vacancies would be a huge challenge. To the best of our knowledge, there has been no report about yttrium doped hedgehog-like CeO_2 obtained by facile controlled synthesis so far.

Herein, we report for the first time a facile and feasible approach to prepare yttrium doped hedgehog-like hierarchical structure CeO_2 by a simple template-free hydrothermal technique using simple inorganic salts $Ce(NO_3)_3$, $Y(NO_3)_3$ and Na_3PO_4 as original materials . The morphology of as-fabricated samples can be controlled by tuning the reaction temperature and reactant concentration.

2. Experimental section

2.1 Preparation. The yttrium doped hedgehog-like hierarchical structure CeO_2 were fabricated through traditional hydrothermal process. All analytical grade origin materials were purchased from Woka Co., Ltd, and were used without any further purification. 0.87g cerium nitrate ($Ce(NO_3)_3·6H2O$) and 0.07g Yttrium nitrate ($Y(NO_3)_3·6H2O$) were dissolved in 100ml of deionized water with vigorous magnetic stirring for 30 minutes at the room temperature. Then 7.7mg sodium phosphate (Na_3PO_4) was added into the aqueous solution. The mixture was stirred continuously for one hour. After that the mixed solution was sealed in a Teflon-lined autoclave and heated at100~250℃ for 12-96 hours. After cooling to the room temperature, a light yellow precipitate was collected by centrifugation and washed with deionized water and ethanol for several times. The target products were obtained after dried in the air at 60℃ for one day.

2.2 Characterizations.

X-ray diffractometer(XRD) with Cu Ka radiation(λ =1.5406Å) was used to identify the crystalline phase carried on Bruker-AXS D8 sss. The crystallite parameters and size were calculated with Rietveld method (TOPAS 4.0). N_2 adsorption and desorption isotherms were recorded at 77K using a Nova 4200e instrument. Precisely weighted the samples and degased at 373K for 3h. The specific surface area was calculated by the 5 points Brunauer-Emmit-Teller theory. Raman analysis was performed using 514 nm excitation laser with 5mW and a air-cooled CCD detector. Raman peak shifts were determined by fitting with Lorentzian and Gaussian

composite function. Morphology and size of as-fabricated products were examined by the field emission scanning electron microscope (FESEM) (Hitachi, S-4800, 15KV) ,high resolution transmission electron microscope (HRTEM) and HADDF-STEM(FEI, Tecnai G2 F30 S-TWIN, 300KV).

2.3 Photocatalytic Evaluations.

UV lighter using black light (UVP, XX-15BLB) can be used in order to remove the possible organic adsorbed on the samples surface more than one week before photocatalytic activity evaluation. The photocatalytic activity of as-fabricated sample was assessed by abilities of decomposition acetaldehyde. Twenty milligrams of powder was spread on the bottom of a glass dish, and the glass dish was placed in a Tedlar bag (AS ONE Co. Ltd.). 500 ppm of acetaldehyde was injected into the bag accompanied with 125 cm^3 artificial air. Then, the bag, which was fabricated above, was put into a dark place at room temperature for 2 hours with the purpose of reaching adsorption equilibrium A light-emitting diode (LED; Epitex, L365), which emitted light at wavelengths of ca. 365 nm, was used as a light source, and its intensity was controlled by 0.9 mW cm^{-2}. The concentration of generated CO_2 was monitored by gas chromatography (Shimadzu GC-8A, FID detector) equipped with a Porapak N packed column and a methanizer (GL Science, MT-221) as a function of irradiation time.

3. Results and discussion

3.1 structure characterization

Typical X-ray diffractometer (XRD) patterns of obtained samples at different conditions are given in the Fig.1.(A)-(D). All the diffraction lines could be indexed to the phase of ceria with the cubic fluorite structure (JCPDS No. 43-1002). The sharp diffraction peaks from all samples suggest a high crystallinity of fabricated samples, and no impurities peaks appeared indicating that reaction time, amount of mineralizer(Na_3PO_4) and concentration of dopant (yttrium nitrate) have no effect on crystalline phase purity of products. The relative intensity of each peak does not change, suggesting that there is no preferred orientation. A weak peak at $2\theta=31.38^0$ assigned to Ce (PO_4)(111) can be seen in the pattern according to the Fig.1.(D) . The results shows that part of Ce^{3+} reacted with PO_4^{3+} in the solution directly to form $CePO_4$ precipitation instead of occur the oxidation to form CeO_2 owing to lower reaction temperature(below 170℃). With increasing the temperature, the impurity crystal phase cerium phosphate disappeared. This phenomenon can be explained that high temperature is beneficial for Ce^{3+} to Ce^{4+}oxidation reaction.

Rietveld Refinements were also carried out according the diffraction lines by varying parameters such as background, unit cell, and isotropic thermal parameters. When reaction temperature and time are changed while maintained the amount of dopant, the variations of lattice value (a=5.30±0.006 Å) are smaller. However, the lattice parameter shows significant variation for as-fabricated samples accompany with dopant stoichiometry changing. The unit cell value a change from 5.33052 to 5.2751 Å (See the Table 1). It can be clearly find that lattice value (a) after doped are smaller than the bulk CeO2 lattice parameter value a=5.41048 Å even though the space group is still Fm-3m before and after doped. It reveals that yttrium have partially substituted cerium ions and introduced into the interior lattice, keeping the ceria cubic fluorite structure instead of forming Y_2O_3-CeO_2 composite. In addition, a linear relationship could be drawn between the lattice value and the amount of doping. In other words, the amount of dopant plays a definitive role in determining ceria lattice parameters. Yttrium enters into the crystal lattice and

substitute cerium ions of crystal lattice. Consequently the crystal lattice would contract owing to an increase in oxygen vacancies concentration with increasing Yttrium content, in spite of the ionic radius of Yttrium is larger than cerium (1.019 and 0.97 Å, respectively). Particles sizes (D) of as-fabricated samples are also be achieved by Whole Pattern Profile fitting instead of single peak refinement (Scherrer formula). D values randomly distributed between the 20-60 nm. Comparison of our results with those reported in previous studies[8, 18, 19]allow us to draw a conclusion that the yttrium have enter into the crystal lattice resulted in the unit parameters variation and particles size do not have effect on the lattice expansion or contraction on certain level.

Raman technology is considered to serve as a very efficiency and nondestructive technique for the characterization of ceria nanoparticles and its derivative. Raman spectral of as-fabricated samples at various experiment conditions are collected in Fig.2 (A)-(D). A strong Raman shift at ~460cm^{-1} and a relatively weak shift at ~600cm^{-1} can be detected for the spectrum. The shift at ~460cm^{-1} can be assigned to the F2g vibration of the fluorite-type lattice and it can be considered the symmetric stretching mode of the oxygen atoms around cerium ions, the molecule retains its tetrahedral symmetry throughout. Based on the Previous literatures[20-22]and our own studies, a weak and less prominent band near ~600Cm^{-1} can be attribute to a nondegenerate longitudinal optical mode caused by local Ce-O (R_{Ce-O})bond symmetry stretch. Previous papers have reported that not all cerium ions show Ce^{4+}chemical valence in lattice; small cerium ions show Ce^{3+}. In order to maintain the particles electrically neutral, the lattice oxygen would escape from the structure and finally result in the formation of intrinsic oxygen vacancies. Oxygen vacancies perturb the local Ce-O bond symmetry. A new and weak Raman shift at ~530cm^{-1}, which cannot be detected on Raman spectral of pure CeO_2, can be observed from the Fig.2.(C) inset graph which is attributed to extrinsic oxygen vacancies caused by doping(R_{dopant}). As a dopant, yttrium ionic enters the cubic fluorite lattice of CeO_2 and substituted Cerium. In order to maintain electronic neutrality, doping cation showing different valence states with Ce^{4+}, and part of oxygen would also escape from lattice to form extrinsic oxygen vacancies. Calculated and compared the relativity intensity of Raman shift (F2g, R_{Ce-O} and R_{dopant}) and summarized in the Table1, we can find value of R_{dopant}/F2g rapidly increased at first and then reached an approximate balance with further increase in dopant content. The change trend of value can be attributed to amount of dopant. At the first yttrium ionic was introduced into the bulk CeO_2, and more extrinsic oxygen vacancies obtained. Therefore the value of R_{dopant}/F2g ratio rapidly increased. Due to the number of lattice defects are certain, although excessive dopant added, the number of oxygen vacancies will eventually maintain a certain level so a steady plateau period appeared. This result from the Raman analysis is also consistent with the following activity evaluation.

3.2 Morphology characterization

The morphology and evolution process of as-fabricated products are investigated by the FE-SEM and HR-TEM. Fig.3 (a) displays a panoramic FE-SEM image of yttrium doped CeO_2 particles, which shows the sample is large-scales uniform octahedral with diameters of approximate 200nm. The lattice spacing of the parallel fringes in the inset graph is 0.32nm, corresponding to the (111) plane of FCC CeO_2. In addition, the elements constitution and distribution of the as-fabricated products at different experimental conditions are analyzed by STEM-HAADF image and EDS mapping images. Fig.4 shows that not only cerium can be

detected but also yttrium have be observed, meanwhile yttrium ions are dispersed evenly on the CeO_2 octahedral structure surface and in bulk. Herein we can draw a conclusion that yttrium has enter into the lattice and doped the parts of cerium successfully. And elements constitution and distribution results are well consistent with the XRD and Raman analysis. Fig.3 (b) shows, with increasing the amount of Na_3PO_4, a small number of nanorods with 50 nm in length and 10nm in diameter growth on the eight octahedral surfaces. The lattice spacing of the parallel fringes in the inset graph are 0.32nm and 0.27nm respectively, corresponding to the (111) plane and (200) plane of FCC CeO_2. The inset shows that the nanorod mainly exposed the (200) planes while the octahedral is exposed the (111) planes. Fig.3(c) reveals that, further increasing the amount of Na_3PO_4, much more nanorod appeared and the octahedral size decreased rapider accompanying with nanorods growth longer. The nanorod length reached about 100 nm holding 10 nm in diameters while octahedral size decreased to 100 nm.

The influence of different doping amount and reaction temperature on morphology was also analyzed by FE-SEM images. Fig.S1 reveals that morphology alters with variation of dopant content. We can observed that, with increasing the amount of $Y(NO_3)_3$, the shape of as-fabricated samples did not change obviously. The morphology and size of products maintain the nanorod on octahedral hierarchical structure. In another word, the amount of dopant has no effect on the morphology and size control. On the contrary, the morphology changed obviously with the reaction temperature. Fig.S2 (a) demonstrates that only octahedral particles can be observed at 150℃ and these particles aggregated due to without surfactant adding. If the reaction temperature was below 150℃, we cannot obtain any precipitation from the solution. With increasing reaction temperature, some short nanoroads appeared on the octahedral surfaces (see the Fig.S2 (b)) and the nanorods are not evenly distributed on the surface. There are some rods on one plane while there is not one rod growthing on the anther plane. When the reaction temperature reached 200 ℃, much more nanorods emerged meanwhile the octahedral size decreased dramatically and the rod became longer in length. Fig.S2 (d) indicates that only the nanorods can be obtained with further increased temperature at the cost of consuming CeO_2 octahedral completely.

Through systematic experiments, it was shown that the hydrothermal temperature and amount of origin sodium phosphate play a vital role in controlling of CeO_2 nanostructures. The as-fabricated samples mainly present octahedral morphology when the PO_4^{3+}concentration is below 0.02 mM and the hydrothermal temperature is under 150℃ due to phosphate group might control the morphology by affect the surface electrostatics potential and energy of octahedral CeO_2. High concentration of PO_4^{3+} will provide more electrostatic potential [23]and high temperature will supply the surface energy on CeO_2 surfaces resulting forming the nanorods plus octahedral hierarchical structure[24, 25]. When the phosphate concentration is exceed 0.85mM and temperature surpass 250℃we can easily obtain nanorods CeO_2 morphologies owing to excessive phosphate groups may restrict the formation of octahedral by steric influence [26]meanwhile high temperature will conducive to the formation of nanorods.

3.3 UV-Vis Diffuse Reflectance Spectra and Band Gap Energy

The UV-vis diffuse reflectance spectral of as-fabricated samples are given in the Fig. 5(a). The optical band gap energy (Eg) can be calculated from plot between E= 1240/λ(nm) [27, 28],where λ is the wavelength corresponding to the absorption, and $[F(R)hv]^{1/2}$ [29, 30]as shown in the Fig.5(b). CeO_2 without doping has absorption at ~380 nm and band gap energy at 3.20 eV,

which originate from the charge-transfer between the O_{2p} and Ce_{4f} states in O^{2-} and Ce^{4+}. Compared with the pure CeO_2, the reflectance decreases and absorption red shifts after yttrium substituted the lattice cerium ions which indicated that the oxygen vacancies increased due to a charge compensation mechanism[31]. Fig.5 (b) clearly reveals that the pure CeO_2 exhibits lower band gap energy compared to yttrium doped ceria and the Eg value are at 3.20 eV and ~3.35 eV respectively.

The subtle differences of band gap of between various morphology of yttrium doped ceria were detected from the plot of K-M curves. Fig. 5(b) indicated that octahedral morphology shows the highest Eg value compared with other shape ceria doped by yttrium. This result is consisted with the Raman analysis and this optical property observation is very important for higher photocatalytic performance.

3.4 Photocatalytic activity for acetaldehyde decomposition

The photocatalytic activities of as-fabricated products were evaluated by measuring CO_2 evolution form the photocatalytic decomposition of acetaldehyde.

Fig.6 (a) shows the time course of CO_2 liberation of the samples at different amount of origin materials Na_3PO_4. Photocatalytic activities enhanced with increasing amount of Na_3PO_4 at the lower content, and higher photocatalytic activity can be observed at 0.47 mM Na_3PO_4 compared with other content. Further increased amount of Na_3PO_4, the photocatalytic activities decreased. Photocatalytic activities changed with the amount of Na_3PO_4 can be attributing to the morphology changing. Only the sample with octahedral plus nanorod morphology has the higher concentration oxygen vacancies than other morphology products owing to hedgehog-like three dimensional hierarchical structure has higher specific surface area(see the Table 1), simultaneously more activity oxygen exists on its surface.

Fig.6 (b) shows the time course of CO_2 liberation of the samples at different reaction temperature. The sample of as-fabricated at 200 ℃ exhibited the highest photocatalytic activities and the photocatalytic activities change trend is similar with the influence of content Na_3PO_4 which is attributed to morphology evolution. That means at higher(>250℃) and lower(<170℃) reaction temperature purely one dimensional (1D) structure, such as octahedral and nanorod, can be obtained. Compared with hedgehog-like 3D hierarchical structure samples, these 1D morphology samples shows lower photocatalytic activities owing to lower concentration of oxygen vacancies and smaller S_{BET}.

Fig.6 (c) shows the time course of CO_2 liberation of the samples of different of dopant concentration. When dopant concentration is low (<0.375 mmol), the as-fabiracted samples shows a low CO_2 liberation rate as the pure CeO_2. However increasing the concentration of dopant, the CO_2 liberation rate improved quickly, which demonstrated that high content dopant is beneficial for photocatalytic activities enhanced. When the content of dopant reached at 0.747 mmol, the fabricated sample showed the highest CO_2 liberation rate and further increasing the concentration of dopant the CO_2 liberation rate decreased.

The photocatalytic activities change trend can be well explained by the oxygen vacancies concentration of the products. Whatever the different morphology samples, such as 1D octahedral, nanorod and 3D hedgehog-like hierarchical structure or different amount of dopant samples, our ultimate destination is to control the oxygen vacancies concentration in the samples. When the fabricated samples are irradiated under the UV light, electrons are excited from the O_{2p} valence

band to conduction band (Ce_{4f}) forming the hole and electron pairs[32].and the holes get trapped on the oxygen ions easily[33, 34]. When the number of oxygen vacancies is higher, the oxygen ion mobility gets higher[35]. The transportation mobility of the lattice oxygen ions is beneficial for the separation of photogenerated electrons and holes. Overall, the photogenerated electron and holes recombination will be restricted in higher oxygen vacancies concentration. Hence 3D hierarchical structure is benefit for higher concentration oxygen vacancies formation and has turned out to possess the best photocatalytic activity.

4. Conclusion

In summary, yttrium doped hedgehog-like hierarchical architectures CeO_2 has been prepared successfully by a simple hydrothermal method. The optimum experiment condition for synthesis of octahedral plus nanorod CeO_2 was found to be 0.47 mM Na3PO4, 0.747mmolY(NO3)3 as origin materials and at 200℃ for 2 hours. Synthetic method is effective and reproducible and can be further expanded to fabricate other rare-earth doped morphology-controlled inorganic nanoparticles materials. Hedgehog-like yttrium doped CeO_2 exhibits an advantage of photocatalytic activities. The results of activity evaluation are mutual consistent with Raman, UV-vis DRS, XRD and SEM analysis. And the photocatalytic activities changing trend have been well explained by the oxygen vacancies derived from the morphology changing and yttrium doping. Consequently, yttrium doped hedgehog-like hierarchical CeO_2 is a promising material for practical application in photocatalytic materials and SOFCs as well as other novel environmental friendly materials.

Acknowledgment

This work was supported by JST PRESTO program and JST ACT-C program.

Figure captions

Fig.1. XRD patterns of as-fabricated samples

Fig.2. Raman spectra of as-fabricated samples

Fig.3. FE-SEM and HR-TEM images of as-fabricated samples at different concentration of Na_3PO_4 (a)-(A) 0.20 mM, (b)-(B) 0.47 mM and (c)-(C) 0.85mM.

Fig.4. HAADF-STEM and EDS mapping images of as-fabricated samples.

Fig.5. Uv-vis diffuse reflectance spectra of different morphology samples.

Fig.6. Time course of CO_2 liberation from acetaldehyde decomposition of as-fabricated samples

Table.1 Relevant data of as-fabircated samples used in the work.

Fig.S1. FE-SEM images of as-fabricated samples at different content of dopant (a)0.05 mmol, (b)0.102 mmol, (c)0.375 mmol, (d) 0.747 mmol,(e) 0.91 mmol and (f)1.2 mmol.

Fig.S2. FE-SEM images of as-fabricated samples at different reaction temperature (a) 150℃, (b)170℃, (c)200℃ and (d)250℃.

References:

[1] K. Zhou, Z. Yang, S. Yang, Chemistry of Materials 19 (2007) 1215-1217.

[2] H. Imagawa, A. Suda, K. Yamamura, S. Sun, The Journal of Physical Chemistry C 115 (2011) 1740-1745.

[3] L. Yan, R. Yu, J. Chen, X. Xing, Crystal Growth & Design 8 (2008) 1474-1477.

[4] R.K. Pati, I.C. Lee, K.J. Gaskell, S.H. Ehrman, Langmuir 25 (2008) 67-70.

[5] Z.-L. Wang, G.-R. Li, Y.-N. Ou, Z.-P. Feng, D.-L. Qu, Y.-X. Tong, The Journal of Physical Chemistry C 115 (2010) 351-356.

[6] Z. Wang, Z. Quan, J. Lin, Inorganic Chemistry 46 (2007) 5237-5242.

[7] S. Kitano, N. Murakami, T. Ohno, Y. Mitani, Y. Nosaka, H. Asakura, K. Teramura, T. Tanaka, H. Tada, K. Hashimoto, H. Kominami, The Journal of Physical Chemistry C 117 (2013) 11008-11016.

[8] C. Paun, O.V. Safonova, J. Szlachetko, P.M. Abdala, M. Nachtegaal, J. Sa, E. Kleymenov, A. Cervellino, F. Krumeich, J.A. van Bokhoven, The Journal of Physical Chemistry C 116 (2012) 7312-7317.

[9] M. Jobbágy, F. Mariño, B. Schönbrod, G. Baronetti, M. Laborde, Chemistry of Materials 18 (2006) 1945-1950.

[10] H. Xiao, Z. Ai, L. Zhang, The Journal of Physical Chemistry C 113 (2009) 16625-16630.

[11] F. Dvořák, O. Stetsovych, M. Steger, E. Cherradi, I. Matolínová, N. Tsud, M. Škoda, T. Skála, J. Mysliveček, V. Matolín, The Journal of Physical Chemistry C 115 (2011) 7496-7503.

[12] Q. Zhang, B. Xu, S. Yuan, M. Zhang, T. Ohno, Materials Letters 121 (2014) 109-112.

[13] Z. Yang, D. Han, D. Ma, H. Liang, L. Liu, Y. Yang, Crystal Growth & Design 10 (2009) 291-295.

[14] L.-W. Qian, X. Wang, H.-G. Zheng, Crystal Growth & Design 12 (2011) 271-280.

[15] S.L. Mitchell, J. Guzman, Materials Chemistry and Physics 114 (2009) 462-466.

[16] L.-S. Zhong, J.-S. Hu, A.-M. Cao, Q. Liu, W.-G. Song, L.-J. Wan, Chemistry of Materials 19 (2007) 1648-1655.

[17] Z.-Y. Pu, X.-S. Liu, A.-P. Jia, Y.-L. Xie, J.-Q. Lu, M.-F. Luo, The Journal of Physical Chemistry C 112 (2008) 15045-15051.

[18] A.E. Baranchikov, O.S. Polezhaeva, V.K. Ivanov, Y.D. Tretyakov, CrystEngComm 12 (2010) 3531.

[19] C.-Y. Cao, Z.-M. Cui, C.-Q. Chen, W.-G. Song, W. Cai, The Journal of Physical Chemistry C 114 (2010) 9865-9870.

[20] Y. Lee, G. He, A.J. Akey, R. Si, M. Flytzani-Stephanopoulos, I.P. Herman, Journal of the American Chemical Society 133 (2011) 12952-12955.

[21] S. Chang, M. Li, Q. Hua, L. Zhang, Y. Ma, B. Ye, W. Huang, Journal of Catalysis 293 (2012) 195-204.

[22] B.M. Reddy, A. Khan, Y. Yamada, T. Kobayashi, S. Loridant, J.-C. Volta, Langmuir 19 (2003) 3025-3030.

[23] G. Cornelis, B. Ryan, M.J. McLaughlin, J.K. Kirby, D. Beak, D. Chittleborough, Environmental Science & Technology 45 (2011) 2777-2782.

[24] D.R. Mullins, P.M. Albrecht, T.-L. Chen, F.C. Calaza, M.D. Biegalski, H.M. Christen, S.H. Overbury, The Journal of Physical Chemistry C 116 (2012) 19419-19428.

[25] Z.L. Wang, X. Feng, The Journal of Physical Chemistry B 107 (2003) 13563-13566.

[26] M. Lin, Z.Y. Fu, H.R. Tan, J.P.Y. Tan, S.C. Ng, E. Teo, Crystal Growth & Design 12 (2012) 3296-3303.

[27] P. Ji, J. Zhang, F. Chen, M. Anpo, The Journal of Physical Chemistry C 112 (2008) 17809-17813.

[28] J. Li, G. Lu, H. Li, Y. Wang, Y. Guo, Y. Guo, Journal of Colloid and Interface Science 360 (2011) 93-99.

[29] Y. Park, S.K. Kim, D. Pradhan, Y. Sohn, Chemical Engineering Journal 250 (2014) 25-34.

[30] C. Karunakaran, P. Gomathisankar, ACS Sustainable Chemistry & Engineering 1 (2013) 1555-1563.
[31] J. Wang, D.N. Tafen, J.P. Lewis, Z. Hong, A. Manivannan, M. Zhi, M. Li, N. Wu, Journal of the American Chemical Society 131 (2009) 12290-12297.
[32] M.a.D. Hernández-Alonso, A.B. Hungría, A. Martínez-Arias, M. Fernández-García, J.M. Coronado, J.C. Conesa, J. Soria, Applied Catalysis B: Environmental 50 (2004) 167-175.
[33] P. Bera, A. Gayen, M.S. Hegde, N.P. Lalla, L. Spadaro, F. Frusteri, F. Arena, The Journal of Physical Chemistry B 107 (2003) 6122-6130.
[34] M.B. Watkins, A.S. Foster, A.L. Shluger, The Journal of Physical Chemistry C 111 (2007) 15337-15341.
[35] B. Murugan, A.V. Ramaswamy, The Journal of Physical Chemistry C 112 (2008) 20429-20442.

Fig 1

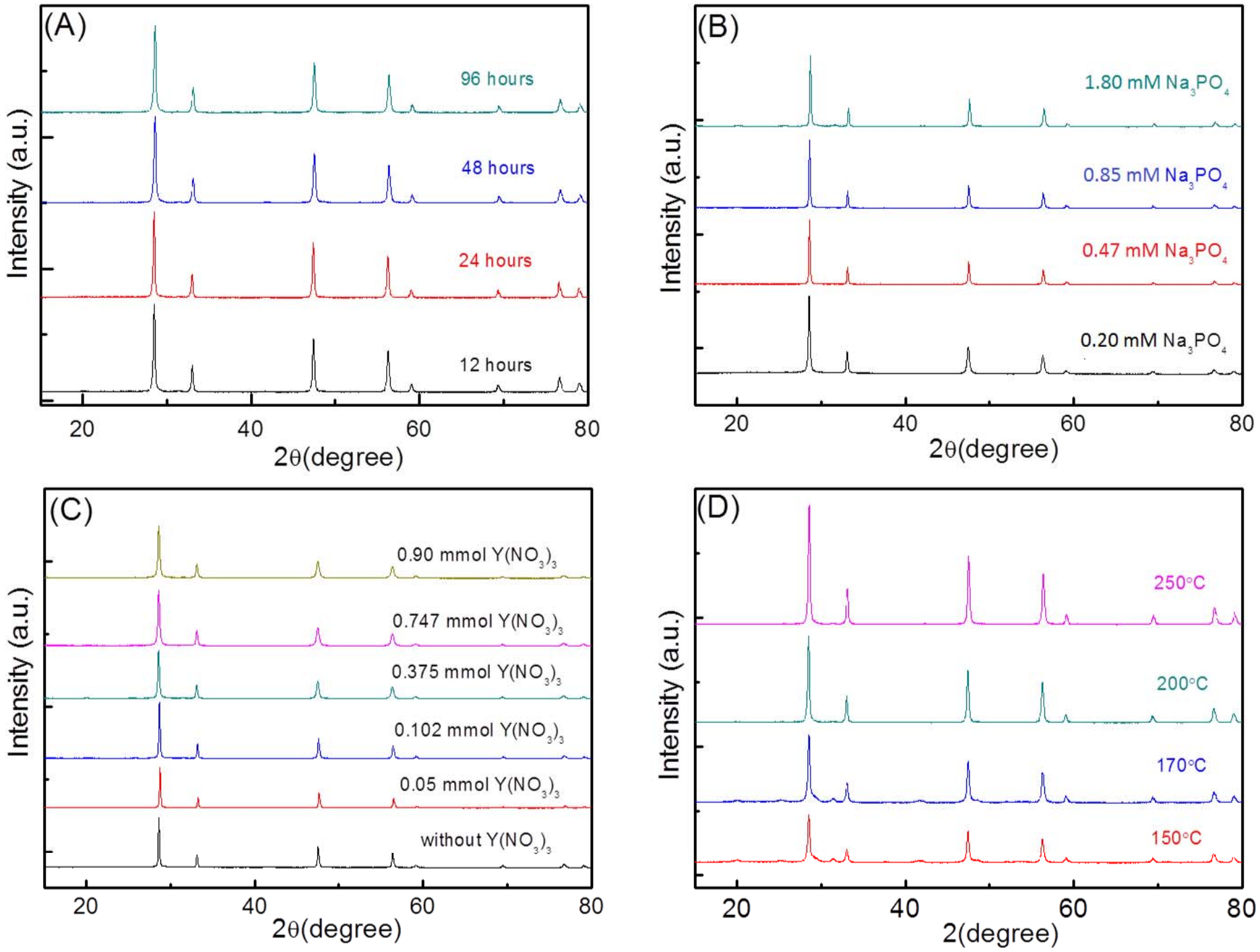
(A)
96 hours
48 hours
24 hours
12 hours
Intensity (a.u.)
20
40
60
80
2θ(degree)
(B)
1.80 mM Na3PO4
0.85 mM Na3PO4
0.47 mM Na3PO4
0.20 mM Na3PO4
Intensity (a.u.)
20
40
60
80
2θ(degree)
(C)
0.90 mmol Y(NO3)3
0.747 mmol Y(NO3)3
0.375 mmol Y(NO3)3
0.102 mmol Y(NO3)3
0.05 mmol Y(NO3)3
without Y(NO3)3
Intensity (a.u.)
20
40
60
80
2θ(degree)
(D)
250°C
200°C
170°C
150°C
Intensity (a.u.)
20
40
60
80
2(degree)

Fig 2

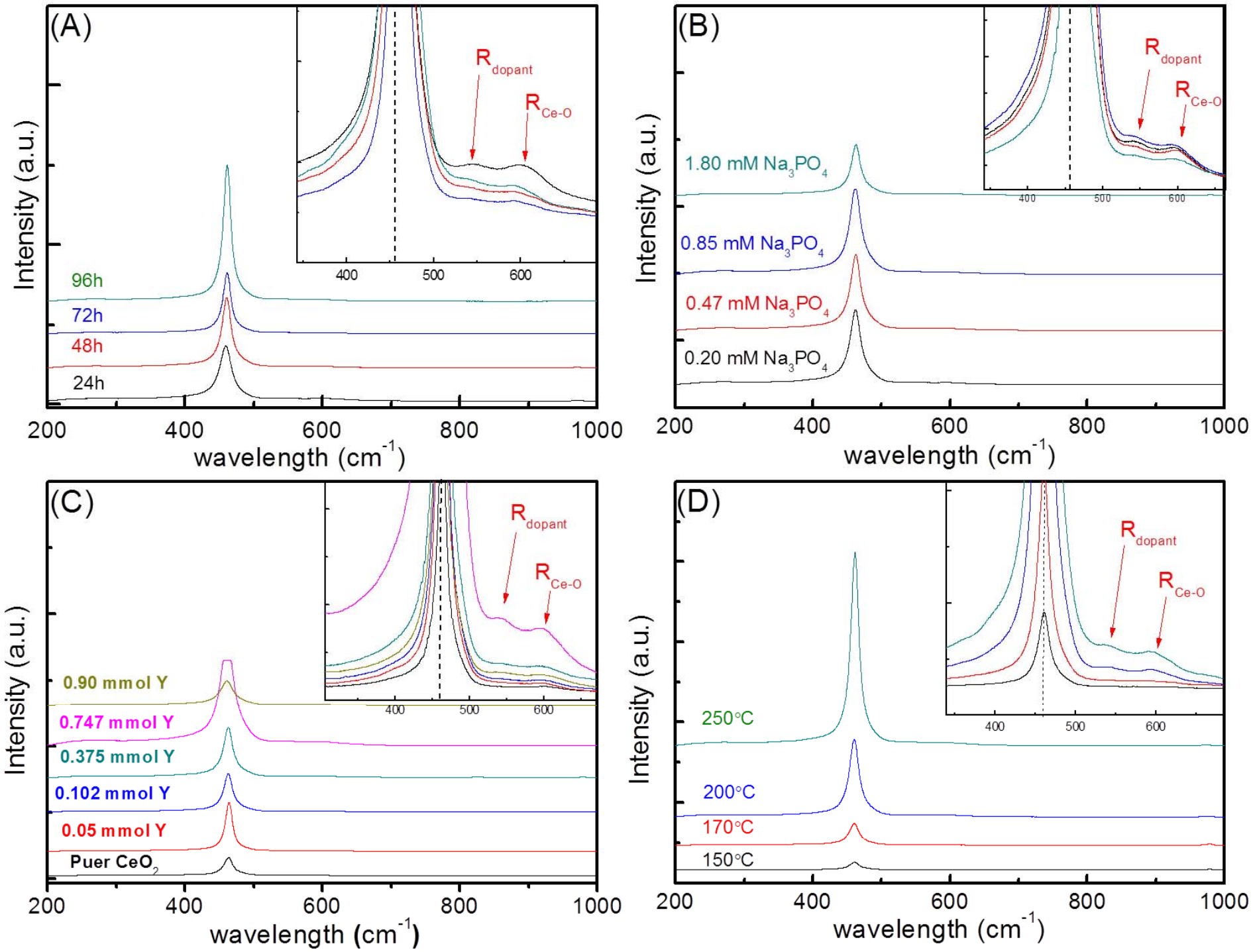
(A)
Intensity (a.u.)
96h
72h
48h
24h
R dopant
R Ce-O
wavelength (cm-1)
(B)
1.80 mM Na3PO4
0.85 mM Na3PO4
0.47 mM Na3PO4
0.20 mM Na3PO4
(C)
0.90 mmol Y
0.747 mmol Y
0.375 mmol Y
0.102 mmol Y
0.05 mmol Y
Puer CeO2
(D)
250°C
200°C
170°C
150°C

Fig 3

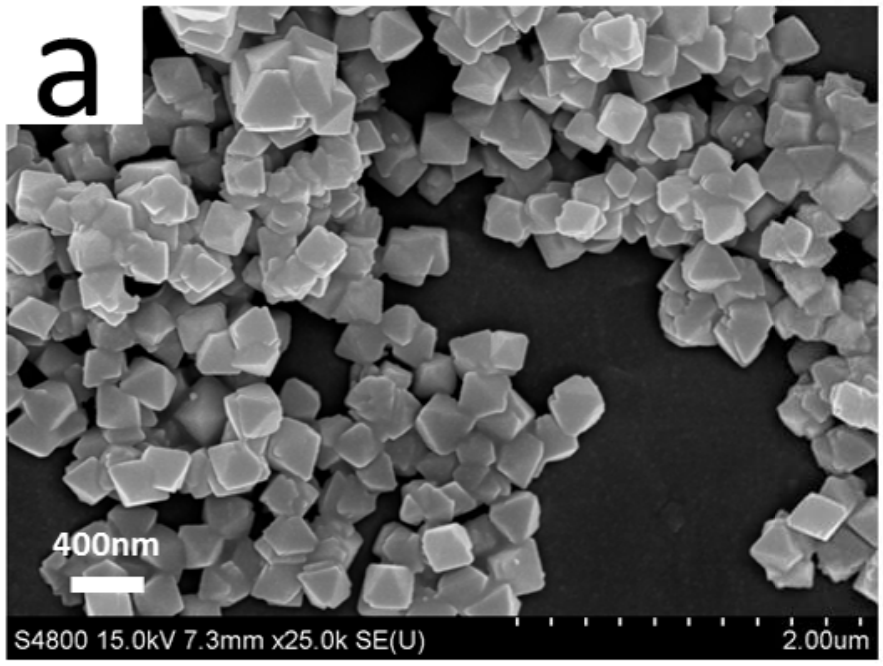
a
400nm
S4800 15.0kV 7.3mm x25.0k SE(U)
2.00um

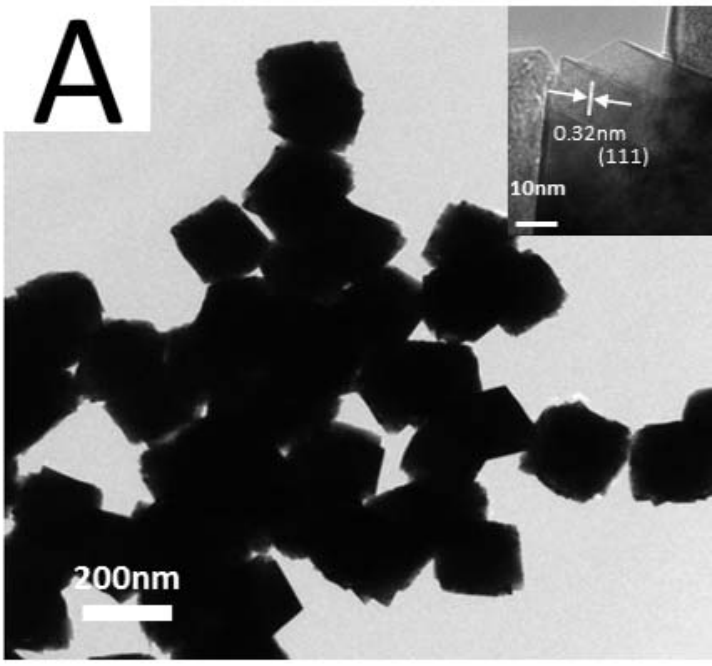
A
0.32nm
(111)
10nm
200nm

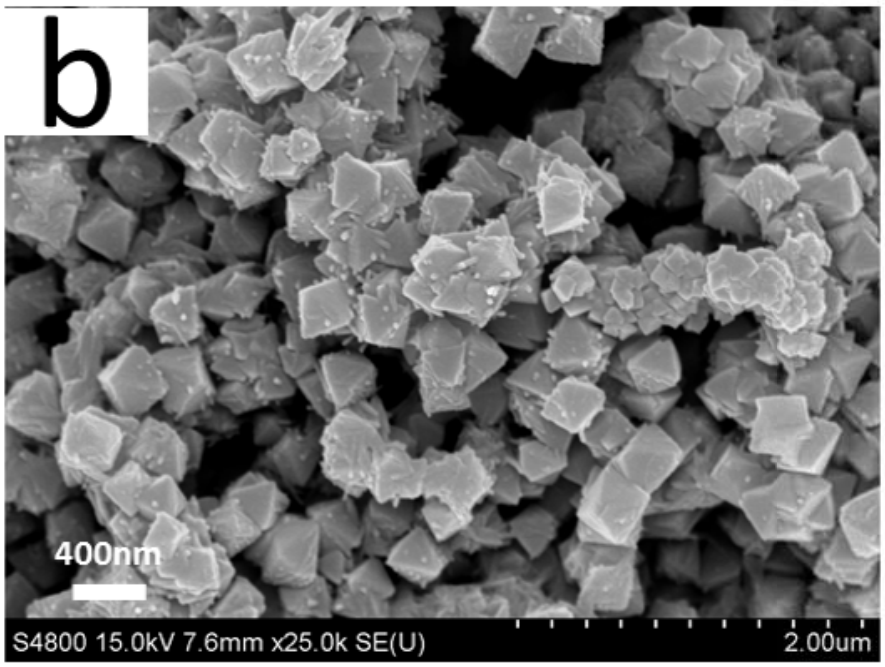
b
400nm
S4800 15.0kV 7.6mm x25.0k SE(U)
2.00um

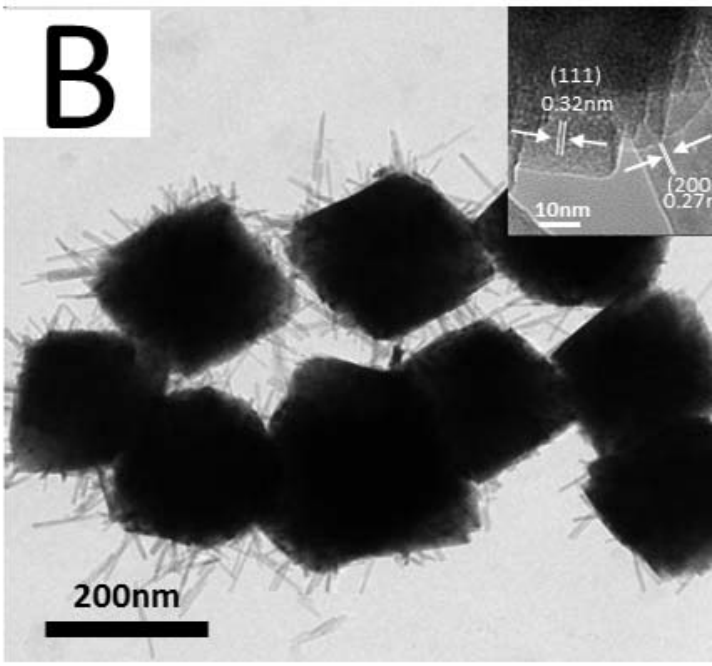
B
(111)
0.32nm
10nm
200nm

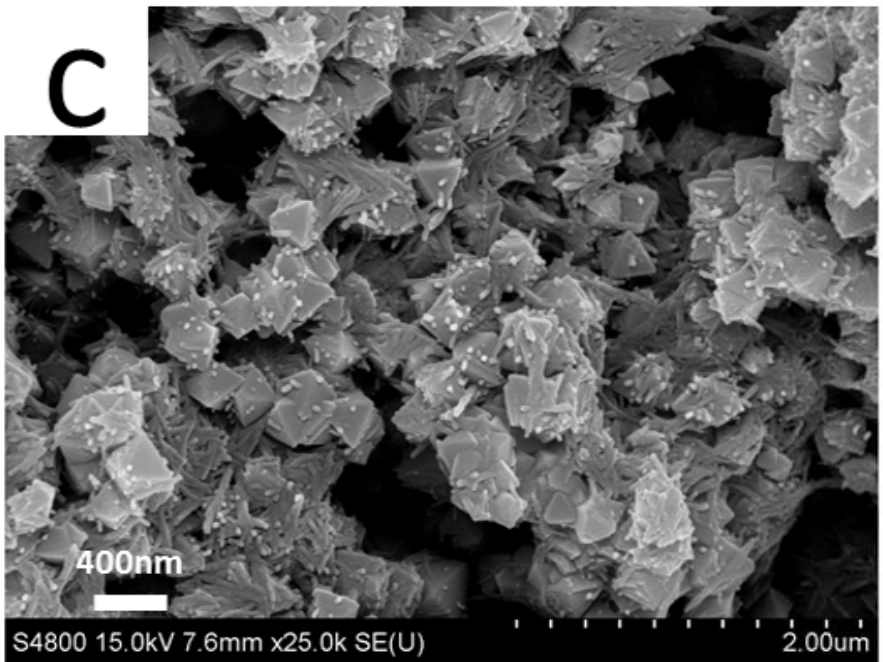
c
400nm
S4800 15.0kV 7.6mm x25.0k SE(U)
2.00um

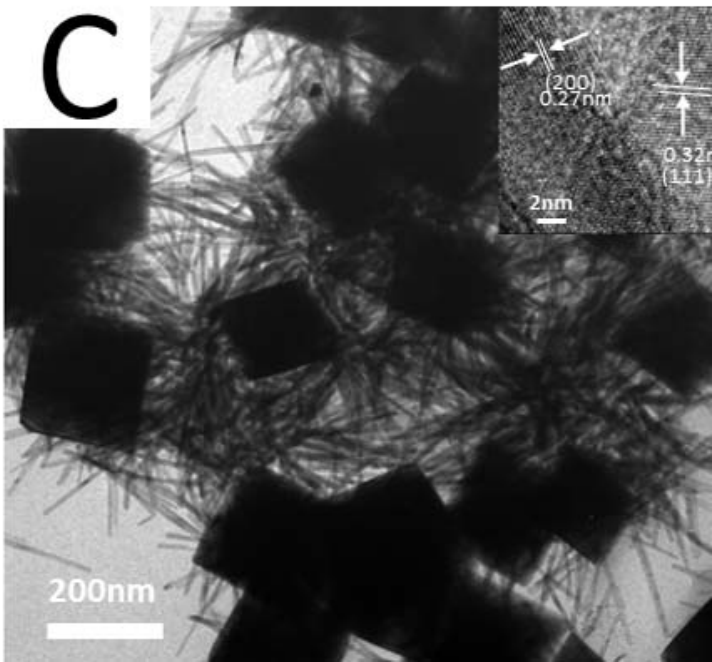
C
(200)
0.27nm
2nm
200nm

Fig 4

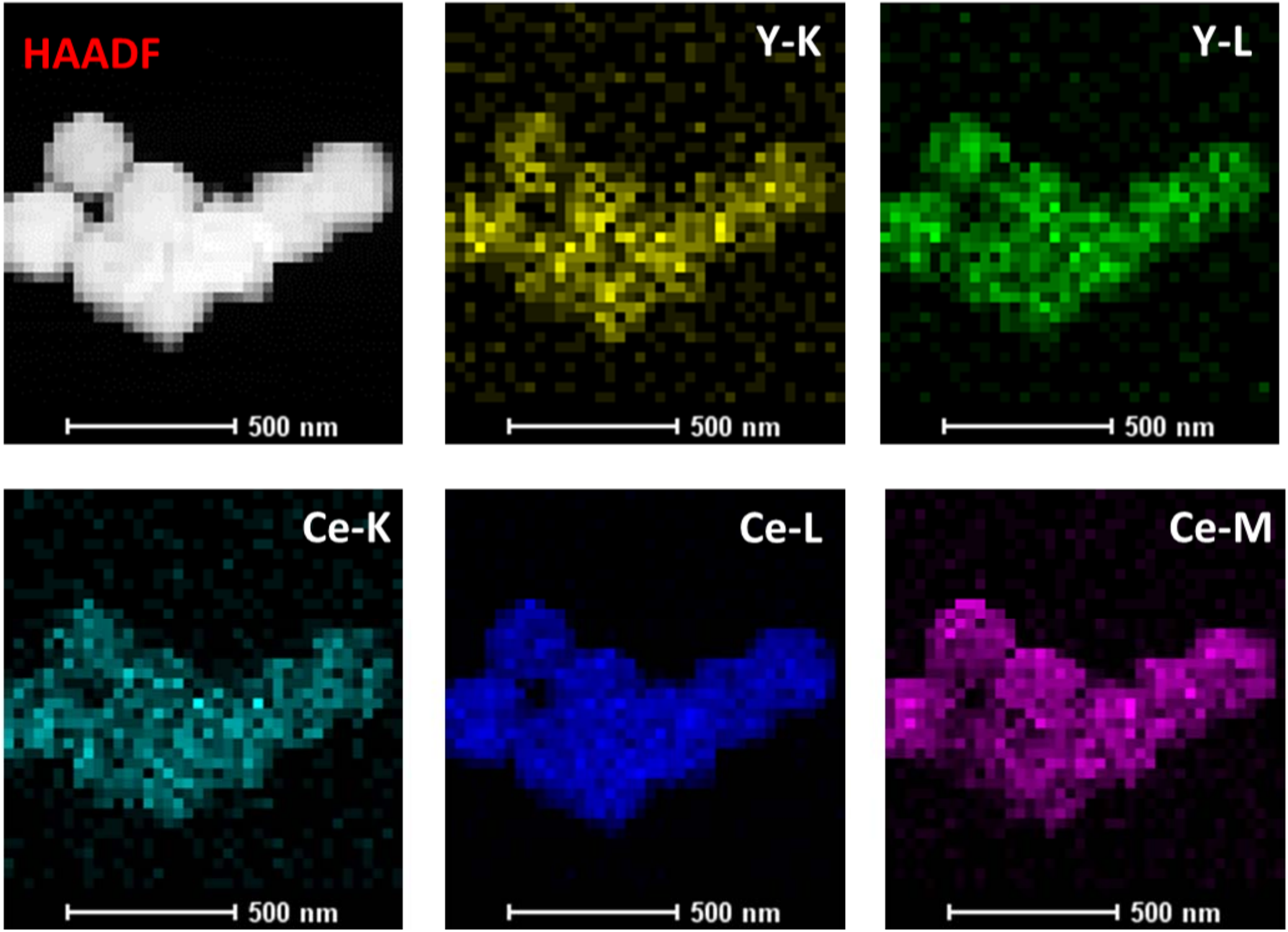

Fig 5

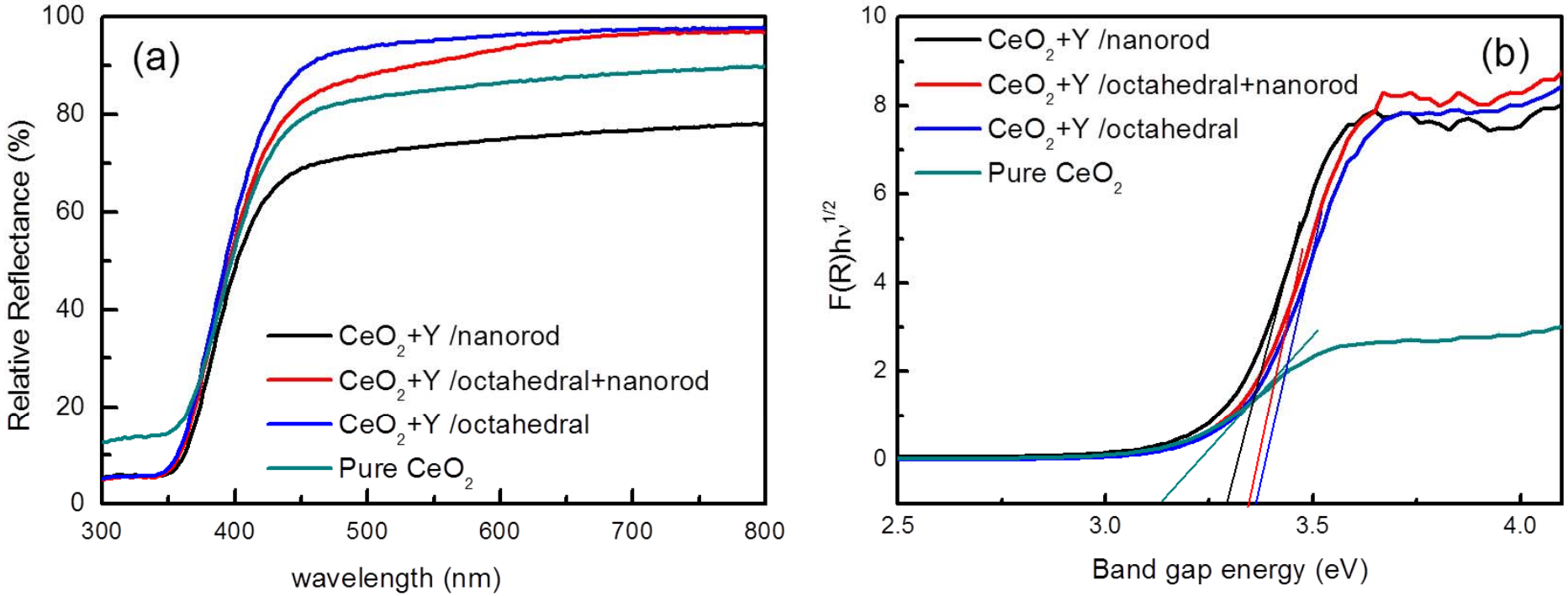
(a)
Relative Reflectance (%)
wavelength (nm)
CeO2+Y /nanorod
CeO2+Y /octahedral+nanorod
CeO2+Y /octahedral
Pure CeO2
(b)
F(R)hν1/2
Band gap energy (eV)

Fig 6

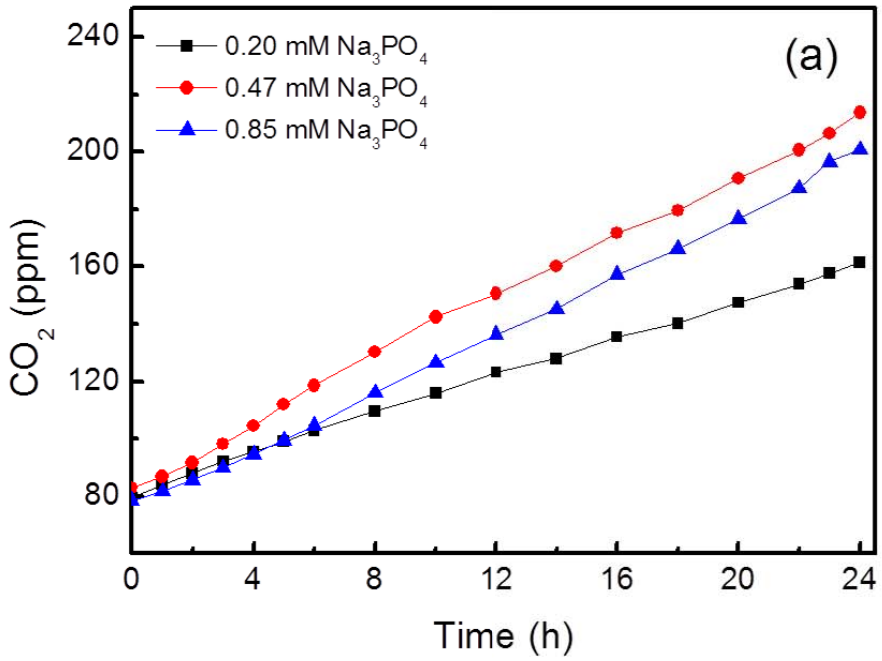
(a)
0.20 mM Na_3PO_4
0.47 mM Na_3PO_4
0.85 mM Na_3PO_4
CO_2 (ppm)
Time (h)

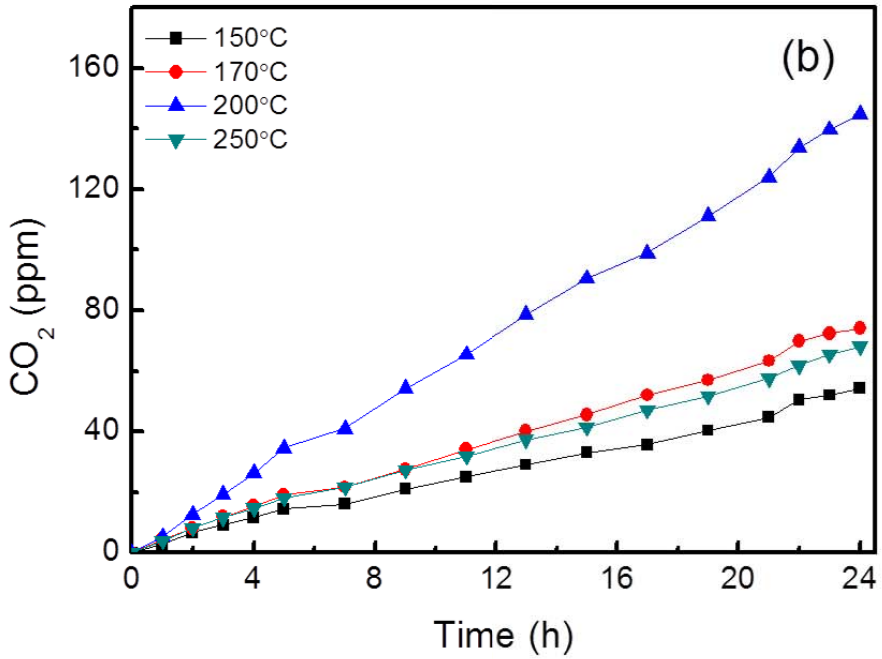
(b)
150°C
170°C
200°C
250°C
CO_2 (ppm)
Time (h)

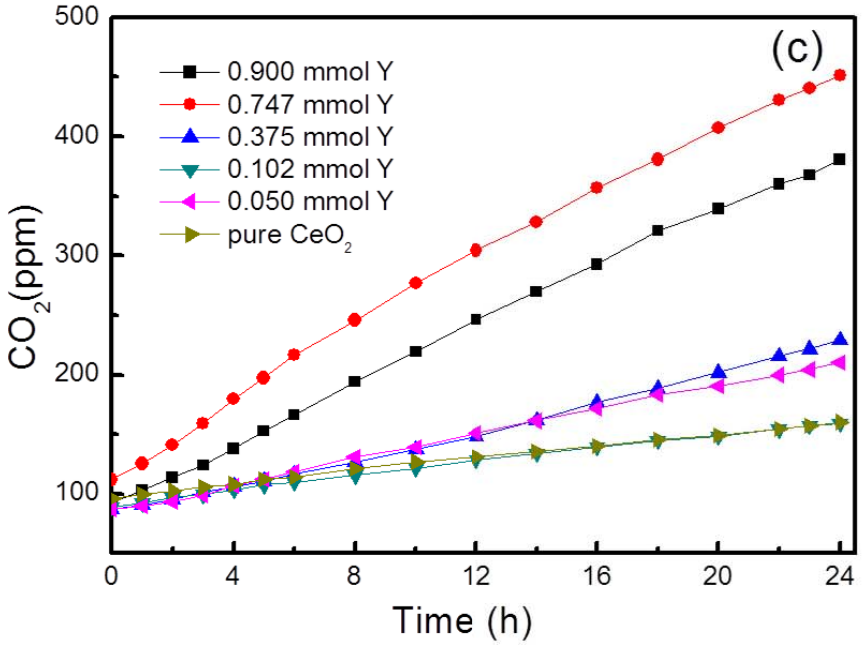
(c)
0.900 mmol Y
0.747 mmol Y
0.375 mmol Y
0.102 mmol Y
0.050 mmol Y
pure CeO_2
CO_2(ppm)
Time (h)

Table.1

sample	Lattice value a (Å)	Particles size D (nm)	R_{dopant}/F2g (%)	S_{BET} (m^2/g)
Pure CeO_2	5.41001	55.987	0	8.132
CeO_2+Y/ octahedral	5.33052	48.162	4.16	23.594
CeO_2+Y/ octahedral+nanrod	5.31606	28.831	4.93	70.405
CeO_2+Y/ nanorod	5.27510	32.833	3.62	49.082

Fig.S1

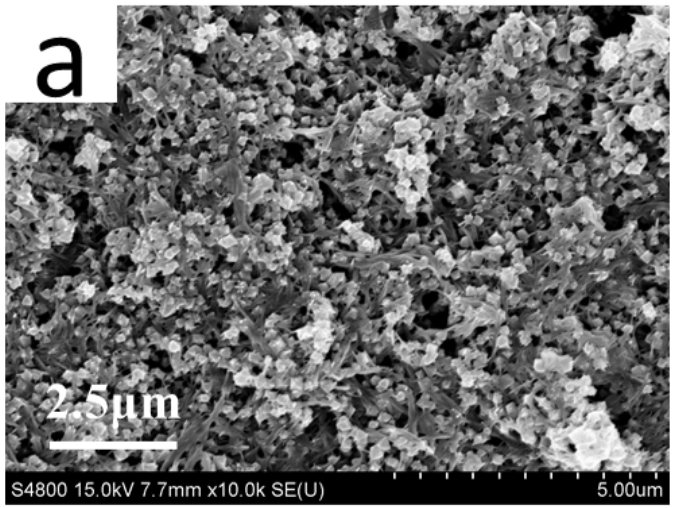
a
2.5μm
S4800 15.0kV 7.7mm x10.0k SE(U)
5.00um

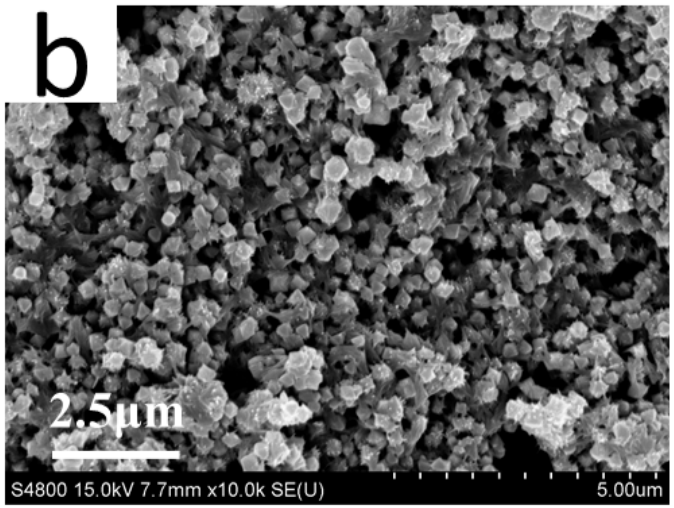
b
2.5μm
S4800 15.0kV 7.7mm x10.0k SE(U)
5.00um

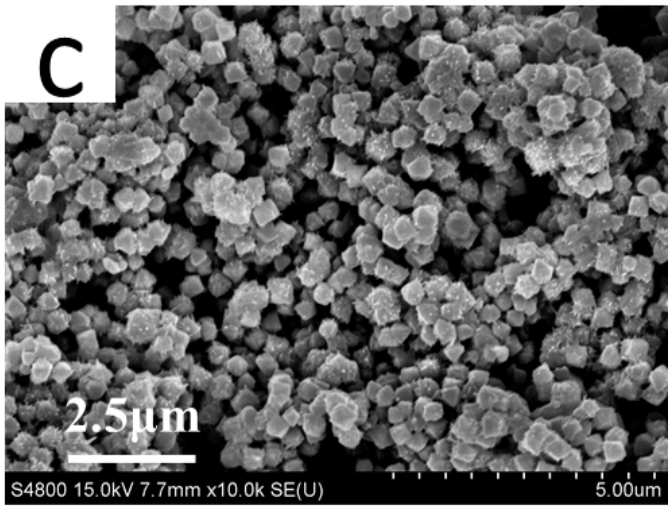
c
2.5μm
S4800 15.0kV 7.7mm x10.0k SE(U)
5.00um

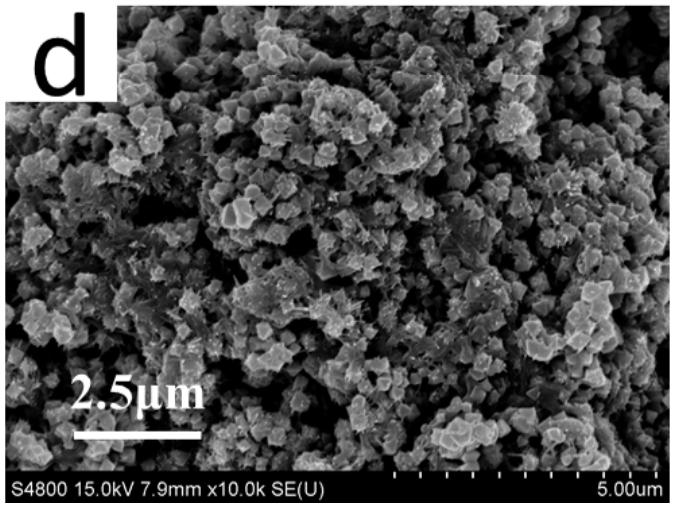
d
2.5μm
S4800 15.0kV 7.9mm x10.0k SE(U)
5.00um

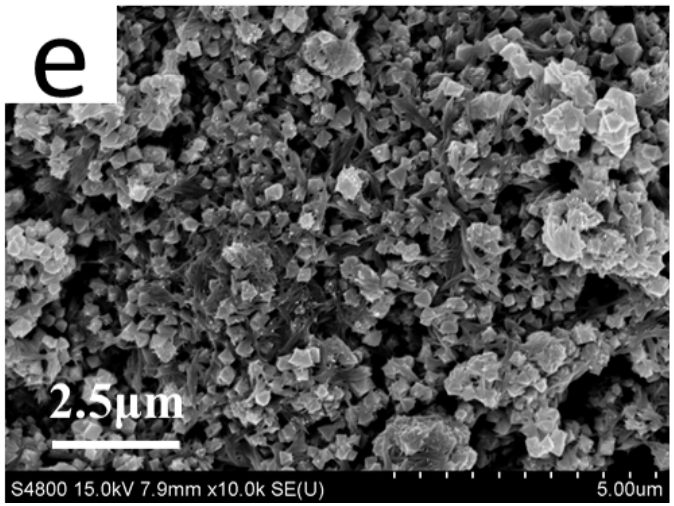
e
2.5μm
S4800 15.0kV 7.9mm x10.0k SE(U)
5.00um

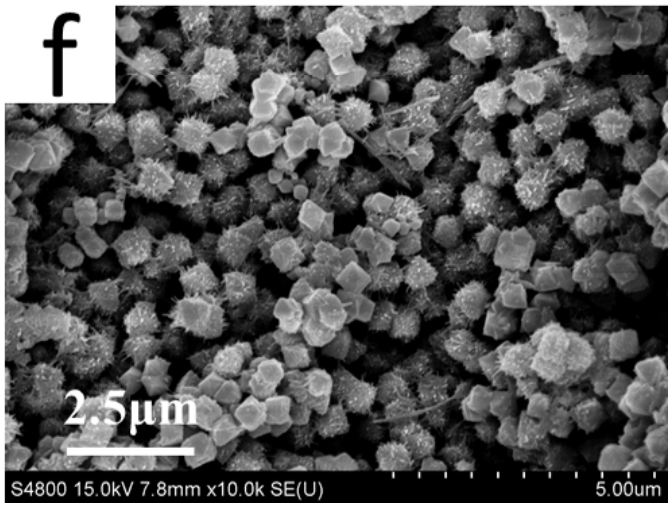
f
2.5μm
S4800 15.0kV 7.8mm x10.0k SE(U)
5.00um

Fig.S2

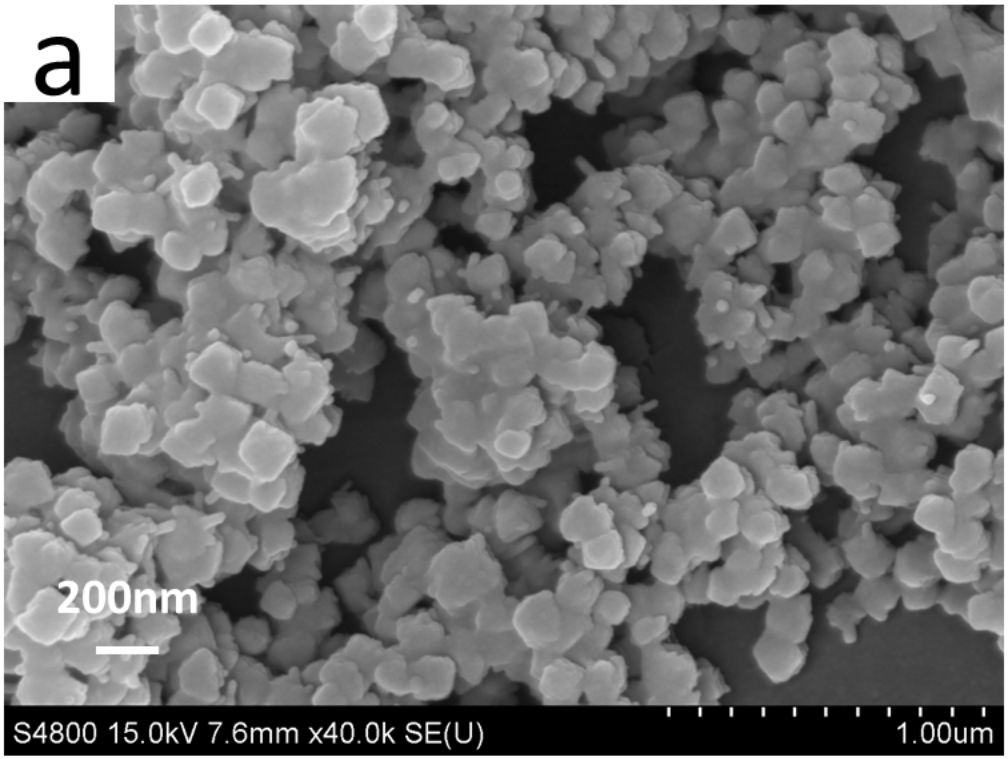
a
200nm
S4800 15.0kV 7.6mm x40.0k SE(U)
1.00um

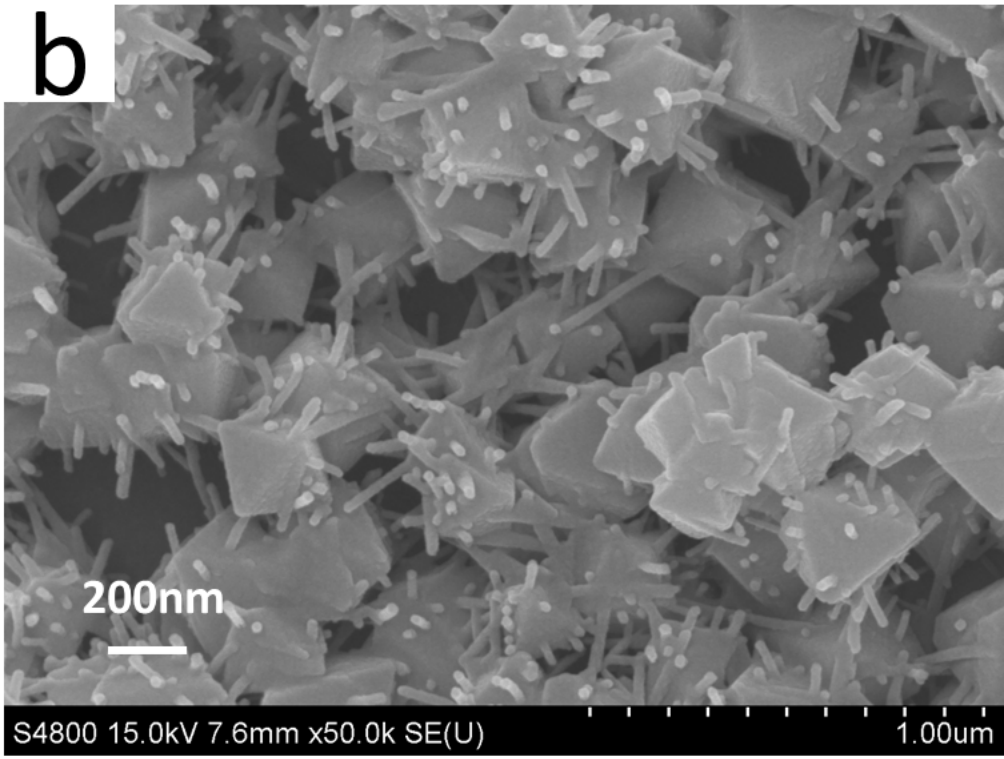
b
200nm
S4800 15.0kV 7.6mm x50.0k SE(U)
1.00um

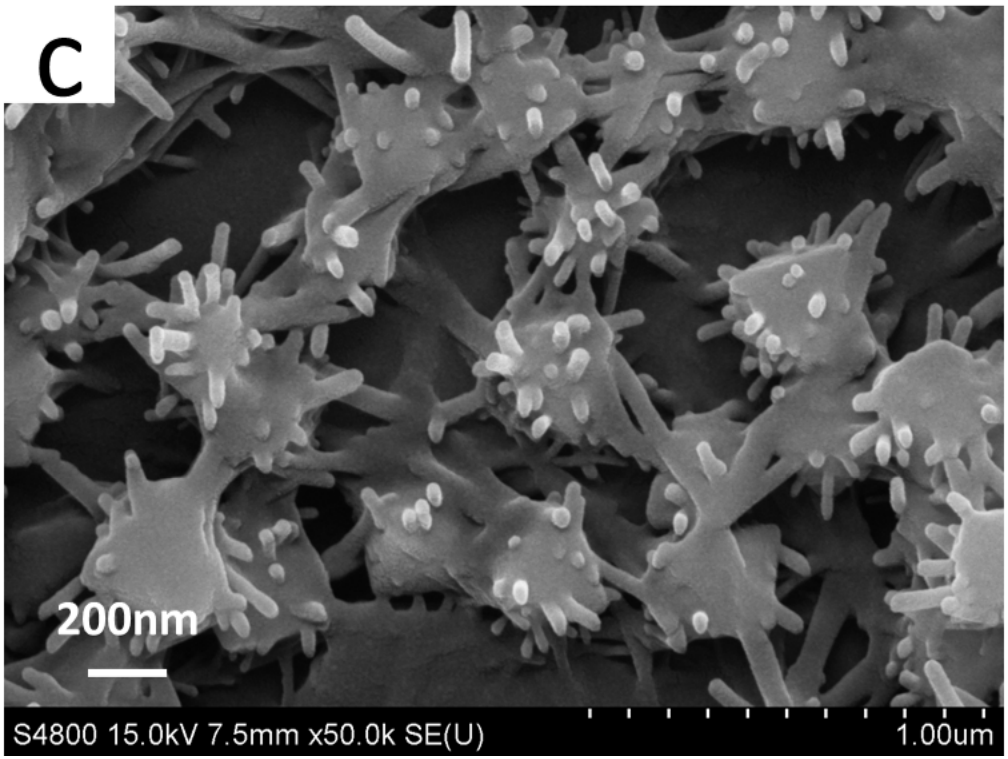
c
200nm
S4800 15.0kV 7.5mm x50.0k SE(U)
1.00um

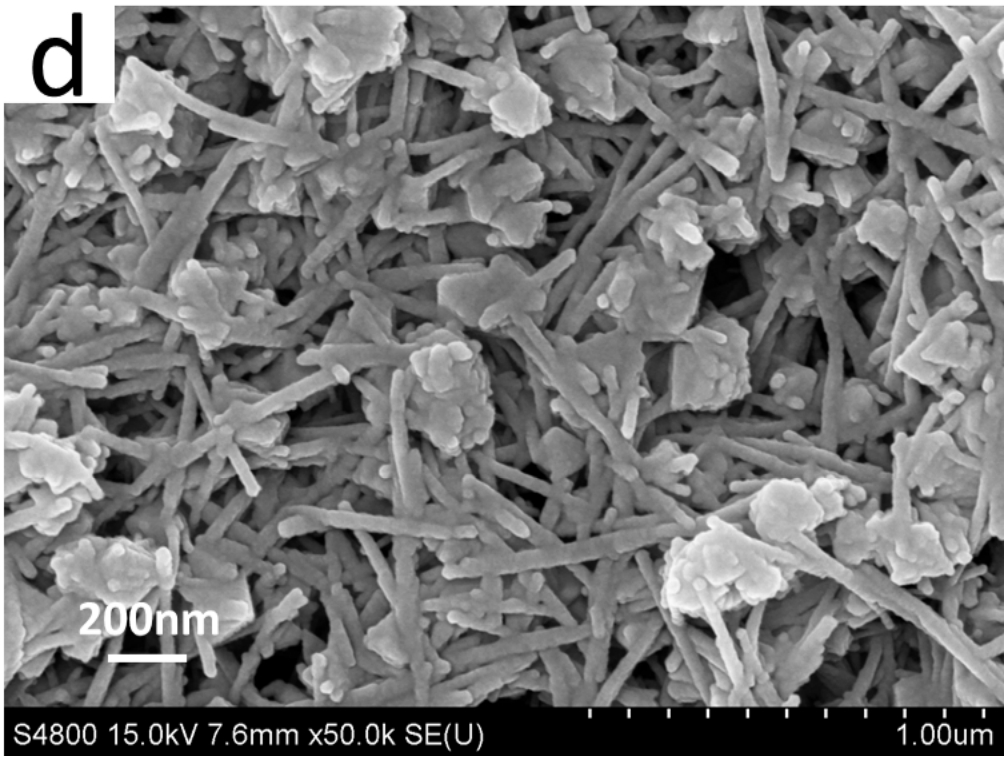
d
200nm
S4800 15.0kV 7.6mm x50.0k SE(U)
1.00um